


Minimizing structural deformation of gold nanorods in plasmon-enhanced dye-sensitized solar cells

Björn Törngren · Simon Sandén · Johan O. Nyman ·
Armi Tiihonen · Hua Jiang · Janne Ruokolainen ·
Janne Halme · Ronald Österbacka · Jan-Henrik Smått 

Received: 4 July 2017 / Accepted: 24 October 2017 / Published online: 3 November 2017
© Springer Science+Business Media B.V. 2017

Abstract Plasmonic metal nanoparticles have shown great promise in enhancing the light absorption of organic dyes and thus improving the performance of dye-sensitized solar cells (DSSCs). However, as the plasmon resonance of spherical nanoparticles is limited to a single wavelength maximum (e.g., ~ 520 nm for Au nanoparticles), we have here utilized silica-coated gold nanorods (Au@SiO₂ NRs) to improve the performance at higher wavelengths as well. By adjusting the aspect ratio of the Au@SiO₂ NRs, we can shift their absorption

maxima to better match the absorption spectrum of the utilized dye (here we targeted the 600–800 nm range). The main challenge in utilizing anisotropic nanoparticles in DSSCs is their deformation during the heating step required to sinter the mesoporous TiO₂ photoanode and we show that the Au@SiO₂ NRs start to deform already at temperatures as low as 200 °C. In order to circumvent this problem, we incorporated the Au@SiO₂ NRs in a TiO₂ nanoparticle suspension that does not need high sintering temperatures to produce a functional photoanode. With various characterization methods, we observed that adding the plasmonic particles also affected the structure of the produced films. Nonetheless, utilizing this low-temperature processing protocol, we were able to minimize the structural deformation of the gold nanorods and preserve their characteristic plasmon peaks. This allowed us to see a clear redshift of the maximum in the incident photon-to-current efficiency spectra of the plasmonic devices ($\Delta\lambda \sim 14$ nm), which further proves the great potential of utilizing Au@SiO₂ NRs in DSSCs.

Electronic supplementary material The online version of this article (<https://doi.org/10.1007/s11051-017-4062-9>) contains supplementary material, which is available to authorized users.

B. Törngren · J.-H. Smått (✉)
Laboratory of Physical Chemistry, Åbo Akademi University,
Porthansgatan 3-5, 20500 Turku, Finland
e-mail: jsmatt@abo.fi

S. Sandén · R. Österbacka
Physics, Åbo Akademi University, Porthansgatan 3-5,
20500 Turku, Finland

J. O. Nyman
Pharmaceutical Sciences Laboratory, Åbo Akademi University,
Artillerigatan 6A, 20520 Turku, Finland

A. Tiihonen · J. Halme
Department of Applied Physics, New Energy Technologies, Aalto
University School of Science, P.O. Box 15100, 00076 Aalto,
Finland

H. Jiang · J. Ruokolainen
Department of Applied Physics, Nanomicroscopy Center, Aalto
University School of Science, P.O. Box 15100, 00076 Aalto,
Finland

Keywords Gold nanorods · Plasmon resonance · Dye-sensitized solar cells · Deformation · Low-temperature processing · Energy conversion · Thin-film photovoltaics

Introduction

During the last decades, the use of photonic materials in order to control light on the nanoscale has contributed greatly to many of the recent advances in science and

technology (Koenderink et al. 2015; Alvarez-Puebla et al. 2010). For instance, metal nanoparticles which display localized surface plasmon resonance (LSPR), i.e., collective oscillations of electrons in the metal upon electromagnetic irradiation (Smith et al. 2015; Zayats and Smolyaninov 2003; Schuller et al. 2010), can be utilized in a wide variety of applications, such as in bioimaging/sensing (Khlebtsov and Dykman 2010; Sotiriou 2013; de Aberasturi et al. 2015; Tokel et al. 2014), photovoltaics (Erwin et al. 2016; Jang et al. 2016; Gu et al. 2012), and photocatalysis (Hou and Cronin 2013; Kale et al. 2014; Long et al. 2015). LSPR occurs at a certain wavelength depending on the type of metal, size and shape of the nanoparticles, as well as on the surrounding medium (Motl et al. 2014). This in turn results in unique properties such as large spectral responses and electromagnetic field enhancements (Murphy et al. 2005). In most applications to date, mainly spherical plasmonic nanoparticles have been used because of the relatively easy synthesis and their good stability in colloidal suspensions. On the other hand, anisotropic particles such as gold nanorods (Au NRs) would offer a larger flexibility in device design due to their unique optical properties (Nikoobakht and El-Sayed 2003; Scarabelli et al. 2015). The elongated shape of the NRs gives rise to an additional LSPR peak at higher wavelengths. These two characteristic peaks for gold nanorods arise from the transverse and longitudinal plasmon modes, which absorb light parallel and perpendicular to the length of the nanorods, respectively. A central problem with utilizing anisotropic plasmonic nanoparticles is their low thermal stability in applications where high-temperature processing is required (e.g., to produce contacts with good charge transport) (Ye et al. 2013). At elevated temperatures, their structure starts to deform in order to lower the overall surface energy (i.e., the nanorods become more spherical). As an effect of the change in aspect ratio of the particles, this deformation will also influence the absorption wavelength (Petrova et al. 2006).

Recently, plasmonic nanoparticles have been utilized in various thin-film photovoltaic technologies to enhance the overall light absorption of the photovoltaic devices (Atwater and Polman 2010; Pillai and Green 2010; Catchpole and Polman 2008). It has been shown that spherical silver or gold nanoparticles added to the active layer can improve the performance of dye-sensitized solar cells (DSSCs) (Brown et al. 2011; Sandén et al. 2015), organic solar cells (Wang et al.

2012), and perovskite solar cells (Carretero-Palacios et al. 2015). The localized surface plasmon resonance generated in metal nanoparticles decay either radiatively by emitting photons or non-radiatively by generating electron-hole pairs (Erwin et al. 2016). The radiative effects will result either in an enhancement of the electromagnetic field, and thus improved absorption around the nanoparticle (near-field), or in light scattering (far-field). It is worth noting that the interaction of the particles with light is a combination of both near-field and far-field effects. However, for spherical particles smaller than 50 nm, the near-field effects are dominant (Liu et al. 2015). Furthermore, coating the metal nanoparticles with a thin metal oxide layer has several important advantages, such as improving the chemical stability and processability as well as allowing better control over the surface modification and functionalization (Standridge et al. 2009; Guerrero-Martínez et al. 2010). When using spherical nanoparticles in photovoltaic devices, the plasmon enhancement typically occurs in the vicinity of the generic LSPR peak of the metal used (i.e., ~ 400 nm for 20 nm Ag particles and ~ 520 nm for 20 nm Au particles). Thus, shifting to anisotropic nanoparticles would allow tailoring of the light absorption to a desired wavelength of choice (e.g., to better fit the absorption range of a certain dye used in a DSSC). There are a few studies where anisotropic plasmonic nanoparticles have been used in photovoltaics (Bai et al. 2014; Chang et al. 2012; Gangishetty et al. 2013). However, possible thermal deformation of the employed anisotropic particles was not addressed in these studies. Neither was the influence of the added particles on the photoanode structure thoroughly studied. In other words, the observed improvements could be due to plasmon effects of nearly spherical particles rather than anisotropic particles or due to structural changes in the photoanode. Careful control over the processing conditions is needed to ensure a minimal restructuring effect on the plasmonic materials.

In the present study, we initially investigate how Au@SiO₂ nanorods are deformed as a function of sintering temperature. Furthermore, we show that by using an Au@SiO₂ nanorod/TiO₂ nanoparticle suspension that does not require high-temperature sintering, we can circumvent the problems with structural deformation. Finally, we demonstrate that the combination of these nanoparticles with the low-temperature suspension can be utilized to produce DSSCs with improved performance in the 500–700 nm wavelength range.

Materials and methods

Chemicals used

Gold(III) chloride hydrate (HAuCl_4 , 99.999% trace metals basis), sodium citrate tribasic dihydrate (99%), L-ascorbic acid (99%), polyvinylpyrrolidone (PVP, MW = 10,000 g/mol), cetyltrimethylammonium bromide, sodium borohydride (98%), titanium(IV) isopropoxide, silver nitrate (>99%), and sodium silicate solution (purum, $\geq 10\%$ NaOH basis, $\geq 27\%$ SiO_2 basis) were purchased from Sigma-Aldrich. (3-Mercaptopropyl)trimethoxysilane (MPTMS, purum 97%) were purchased from Fluka. P25 TiO_2 nanoparticles were purchased from Evonik Degussa. Millipore water was used in the preparation of all aqueous solutions.

Core-shell nanoparticle synthesis

Gold nanorods (Au NRs) were synthesized following the two-step method presented by Nikoobakht and El-Sayed (2003). Briefly, a gold seed solution was first prepared by mixing 5 mL of an aqueous 0.2 M CTAB solution with 0.5 mM HAuCl_4 under stirring. To this mixture, ice-cold 0.01 M sodium borohydride (NaBH_4) solution was added under vigorous stirring, turning the solution from light yellow to brownish yellow. Growth solutions were prepared by adding 5 mL of an aqueous 0.2 M CTAB solution to a varying amount of 4 mM silver nitrate (AgNO_3) solution. The amount of AgNO_3 controls the Au NR aspect ratio, and we used 0.1 mL to produce low aspect ratio nanorods (Au NR-1) and 0.25 mL to make nanorods with a high aspect ratio (Au NR-2) (Pérez-Juste et al. 2005). Thereafter, 5 mL of 1 mM HAuCl_4 was added to both solutions and after gentle mixing, 70 μL of 0.079 M ascorbic acid solution was added. The growth solutions changed color from dark yellow to colorless, indicating the reduction of the gold ions. Finally, 12 μL of the seed solution was added to the growth solutions. The samples gradually changed color during the first 15–30 min, resulting in a dark brown color. The resulting mixtures were kept at 35 °C overnight, thereafter centrifuged and washed with water and ethanol.

In order to provide an insulating and protective coating on the gold nanorods, a thin SiO_2 layer is grown on the gold surface (Törngren et al. 2014). For this purpose,

the method by Obare et al. (2001) was used with slight modifications. Briefly, 200 μL of MPTMS solution (10 μL in 1 mL ethanol) was added to 25 mL of the Au NR solutions and stirred for 20 min. An aqueous solution of sodium silicate (0.54 wt%) was prepared and 800 μL was added to the Au NR suspensions under stirring. The stirring was continued for 20 min and thereafter the mixture was allowed to sit for 12 h. The nanoparticles were thereafter centrifuged and washed with water and ethanol.

The structure and the thermal deformation of the gold nanorods were studied using transmission electron microscopy (TEM). In situ TEM studies were conducted with a JEOL JEM-2200FS operating at 200 kV acceleration voltage, while images of the structure were taken with a JEOL JEM-1400 Plus operating at 120 kV acceleration voltage. The optical properties of the synthesized core-shell nanoparticles were characterized in acetone using UV-vis absorption spectroscopy using a Shimadzu UV-2501PC spectrometer. In order to study the effect of thermal treatment of the core-shell nanoparticles, the particles were drop-casted onto glass slides and characterized using UV-vis spectroscopy using a Perkin-Elmer Lambda 900 with an integrating sphere setup.

Low-temperature TiO_2 suspension formulation

A TiO_2 suspension suitable for low-temperature processing was prepared following a modified method based on work by Zhang et al. (2006) as well as Kim and Hwang (2014). P25 TiO_2 nanoparticles were pre-heated to 450 °C to remove any organic contaminants and absorbed moisture. A suspension of TiO_2 nanoparticles was prepared by mixing 1 g of P25 TiO_2 with 8.5 g of ethanol and 0.14 g of deionized water. This suspension was sonicated with a 50 W sonic horn (Vibra-Cell 50AT, Sonics & Materials Inc.) for 30 min. To this suspension, 0.36 g of titanium isopropoxide was added and mixed with a magnetic stirrer for 4 h to ensure homogeneous mixing. During the preparation, Au@ SiO_2 NRs dispersed in ethanol were added to the suspension so that the total mass of gold in the final film was 2 wt%. TiO_2 films with or without Au@ SiO_2 particles were prepared by dip coating the suspension four times onto FTO glass substrates. After each dipping, the films were dried for 10 min at 120 °C to remove the solvent and to improve the mechanical stability. After

the four dipping cycles, the films were sintered at 200 °C for 30 min.

X-ray diffraction (XRD) was used to study the crystalline nature of the produced films using a Bruker AXS D8 Discover instrument. The film structure was studied by scanning electron microscopy (SEM), using a Zeiss Leo Gemini 1530 instrument. The surface roughness and film thickness on a larger sample size were studied using a custom-built Scanning White-Light Interferometer consisting of a halogen lamp (Osram G4, driven at 5 V, 10 W), a standard 10× Mirau objective (Nikon CF IC Epi Plan DI; Japan) and a piezo translator with 100 μm z-range (Physik Instrumente - type P-721.CDQ). In the receiving part, a black and white CCD camera (Hamamatsu C11440 Orca Flash 2.8, Hamamatsu City, Japan) was used. Atomic force microscopy (AFM) height profiles were used to estimate the final thickness of the produced films utilizing an NTEGRA Prima (NT-MDT) instrument. Furthermore, the BET surface areas of the films were determined using Kr physisorption at 77 K (Autosorb 1, Quantachrome).

DSSC assembly

Photoanodes were made by immersing the reference TiO₂ and the TiO₂/Au@SiO₂ NR composite films in a dye solution containing 3 mM of N719 dye (di-tetrabutylammonium cis-bis(isothiocyanato)bis(2,2'-bipyridyl-4,4'-dicarboxylato)ruthenium(II) in ethanol for 20 h. DSSCs were assembled by sandwiching Himilan spacer films between the photoanodes and Pt-coated FTO glass substrates and injecting the liquid electrolyte (0.1 M lithium iodide, 0.6 M 1,2-dimethyl-3-propylimidazolium iodide, 0.5 M 4-tert butylpyridine, 0.025 M iodine in acetonitrile) between them.

Dye desorption measurements were carried out by immersing the TiO₂ films in an aqueous 0.1 M NaOH solution for 30 min. The desorbed dye solutions were measured with a Shimadzu UV-2501PC spectrometer. A molar absorbance coefficient 13,312 L cm⁻¹ mol⁻¹ at 520 nm for the N719 dye was used in the calculations. The current-voltage (J-V) characteristics of the DSSCs were measured under AM 1.5G irradiation at 100 mW/cm² using a Xe lamp solar simulator (PEC-L01, Peccell). Incident photon-to-current efficiency (IPCE) spectra were measured with a monochromator equipped with a 150 W Xe lamp (QEX7, PV Measurement, Inc.).

Results and discussion

Structural and optical properties of the plasmonic gold particles

The size and shape of the Au NRs were investigated by TEM measurements (see Fig. 1). The width of the nanorods are ~ 20 nm in both cases, while the aspect ratios of the Au NR-1 and Au NR-2 particles are ~ 1.7 and ~ 3.2, respectively. Although the samples show good uniformity in size and shape, some shorter nanorods can also be seen (especially in the Au NR-1 sample). Furthermore, Fig. 1c shows that the gold nanorods have successfully been coated with a 2–3-nm-thin SiO₂ layer. As previously mentioned, a thin insulating SiO₂ shell is needed to protect the gold nanorods from the chemically aggressive electrolyte and to prevent quenching of the generated charges. Based on our previous studies, a silica shell with a thickness in the range of 2–5 nm is optimal for near-field plasmonic enhancement (Sandén et al. 2015). Thinner shells or incomplete coverage can lead to rapid dissolution of the gold nanoparticles in the electrolyte (Törmgren et al. 2014), while thicker shells will decrease the plasmonic effect and its impact on device performance (Wong 2017; Zhang et al. 2016).

The absorption spectra of the pristine and silica-coated gold particles are shown in Fig. 2. The Au NRs have two distinct absorption peaks due to the anisotropic nature of the particles. The transverse peak is fixed at ~ 520 nm, while the longitudinal peak position shifts depending on the particle aspect ratio (length/width). Two types of gold nanorods were synthesized by varying the amount of silver nitrate in the growth solution: one type with the longitudinal peak at 696 nm (Au NR-1) while the other has the peak located at 800 nm (Au NR-2) (see Table 1).

After coating the gold particles with a thin silica layer, the plasmon peaks are slightly red-shifted due to changes in the surrounding dielectric constant (see peak maxima values in Table 1) (Bohren and Huffman 2004). As both samples showed good chemical stability in electrolyte solution, we conclude that the SiO₂ shells are thick enough and defect free around the gold cores. Previously, we have shown that Au cores with incomplete silica shells rapidly dissolve in I⁻/I₃⁻ electrolyte solution leading to a visible change in color of the particle solution (Törmgren et al. 2014). The noticeable increase in the absorption in the 300–400 nm range after coating

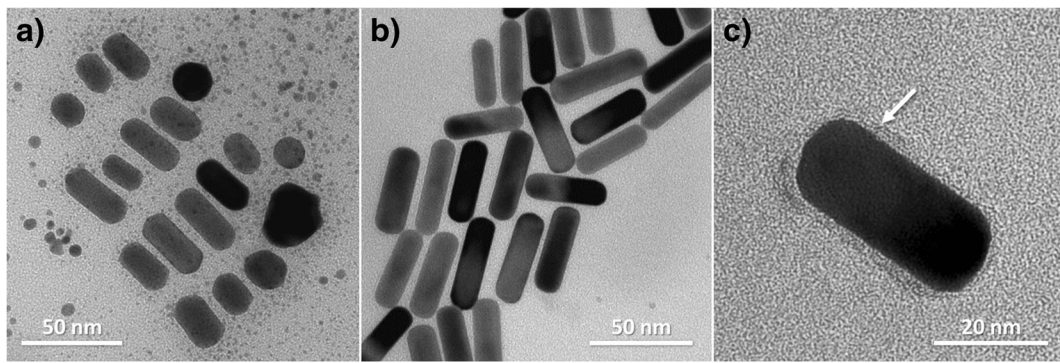


Fig. 1 TEM images of the two gold nanorod samples used in this study: **a** Au NR-1 and **b** Au NR-2. **c** Shows the thin SiO₂ coating for the Au@SiO₂ NR-1 sample

the Au NR samples is most likely due to increased absorption by the silica coating (Cong et al. 2010).

The effects of thermal treatment on the core-shell particles were studied by drop casting the solutions on a glass slide and heating the samples to different temperatures. Absorption spectra of the Au@SiO₂ NR-1 sample heated to different temperatures are shown in Fig. 3. As there is no substantial effect on the longitudinal plasmonic peak up to 200 °C (the peak maximum remains at ~ 700 nm), the nanorods can be considered thermally stable up to this temperature. However, at higher temperatures, the longitudinal peak starts to shift to lower wavelengths, indicating that the particles are becoming more spherical. This deformation was further confirmed by TEM measurements using in situ heating (see Fig. S1 in

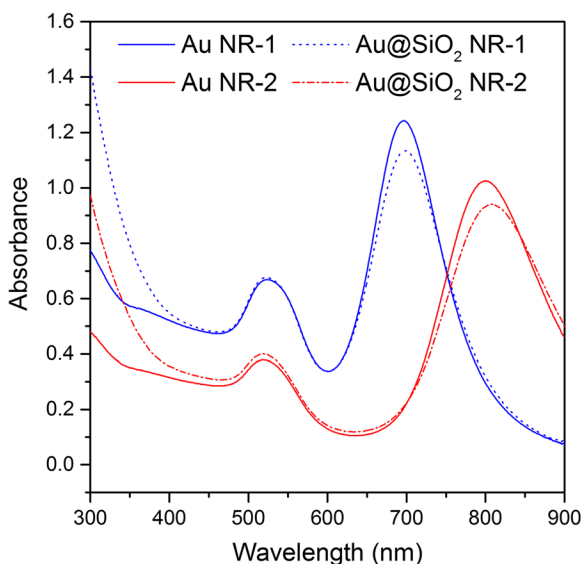


Fig. 2 UV-vis spectra of synthesized gold nanorods before and after SiO₂ coating

the Supplementary Information). At elevated temperatures, the gold nanorods start to soften or melt, and in order to reduce their interfacial energy, the particles lower their aspect ratio. This also influences the optical properties of the Au@SiO₂ NRs (Nikoobakht and El-Sayed 2003). Furthermore, this deformation at elevated temperatures is in good agreement with previous studies on bare Au NRs (Petrova et al. 2006). Thus, in order to fully utilize the plasmonic properties of the Au@SiO₂ NRs in an application, all subsequent processing steps should be carried out at relatively low temperatures (i.e., 200 °C or below). This temperature limit is significantly lower than the commonly used sintering temperatures for the TiO₂ photoanode in DSSCs (~ 500 °C). This fact was not taken into consideration in previous studies where anisotropic metal nanoparticles have been used in plasmon-enhanced DSSCs (Bai et al. 2014; Chang et al. 2012).

Reference TiO₂ and composite TiO₂/Au@SiO₂ NR films

TiO₂ suspensions suitable for dip coating or spray coating in combination with low-temperature sintering were prepared according to previously reported procedures (Zhang et al. 2006; Kim and Hwang 2014). These TiO₂

Table 1 Aspect ratios as well as the longitudinal peak wavelength maxima of the gold nanorods before and after SiO₂ coating, and after embedded in the TiO₂ films

Sample	Aspect ratio	Pristine (nm)	Silica-coated (nm)	In TiO ₂ film (nm)
Au NR-1	1.7 ± 0.5	696	699	630
Au NR-2	3.2 ± 0.3	800	808	730

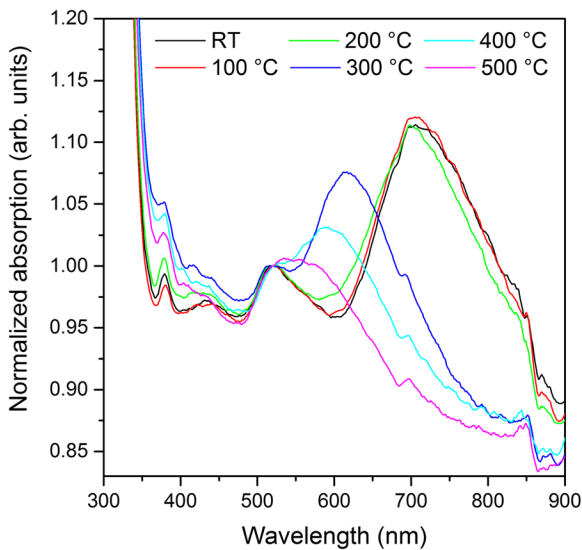


Fig. 3 UV-vis spectra of drop-cast gold nanorods (sample Au@SiO₂ NR-1) heated to different temperatures. The spectra have been normalized at 520 nm

suspensions (with and without added Au@SiO₂ NRs) were dip-coated onto FTO-coated glass substrates and sintered at 200 °C. The dipping/heating cycle was repeated four times to produce thicker films. The interparticle connectivity arises from the sol-gel reaction of titanium isopropoxide with the water in the suspension. XRD was used to detect differences in the crystallinity between the reference TiO₂ sample treated at room temperature, 200 and 500 °C (see Fig. S2 in the Supplementary Information). However, no discernable differences could be observed between the samples indicating that the heating temperature does not have a large influence on the crystallinity of the TiO₂ photoanodes. This is in good agreement with the study by Nakade et al. (2002), where no great difference in the XRD patterns could be seen when annealing similar TiO₂ films consisting of P25 and titanium isopropoxide at different temperatures. The anatase/rutile mass ratio is the same as for the pristine P25 TiO₂ nanoparticles (about 85:15). From the top-view SEM images shown in Fig. 4, almost no noticeable differences can be seen between the reference TiO₂ film and the TiO₂ films with added nanoparticles. All the samples show a similar porous film structure without any larger cracks or aggregates. From the higher magnifications in the insets, it is possible to discern the size of distinct particles (~ 13 ± 2 nm for all three samples). These particles are loosely aggregated into an open porous network where

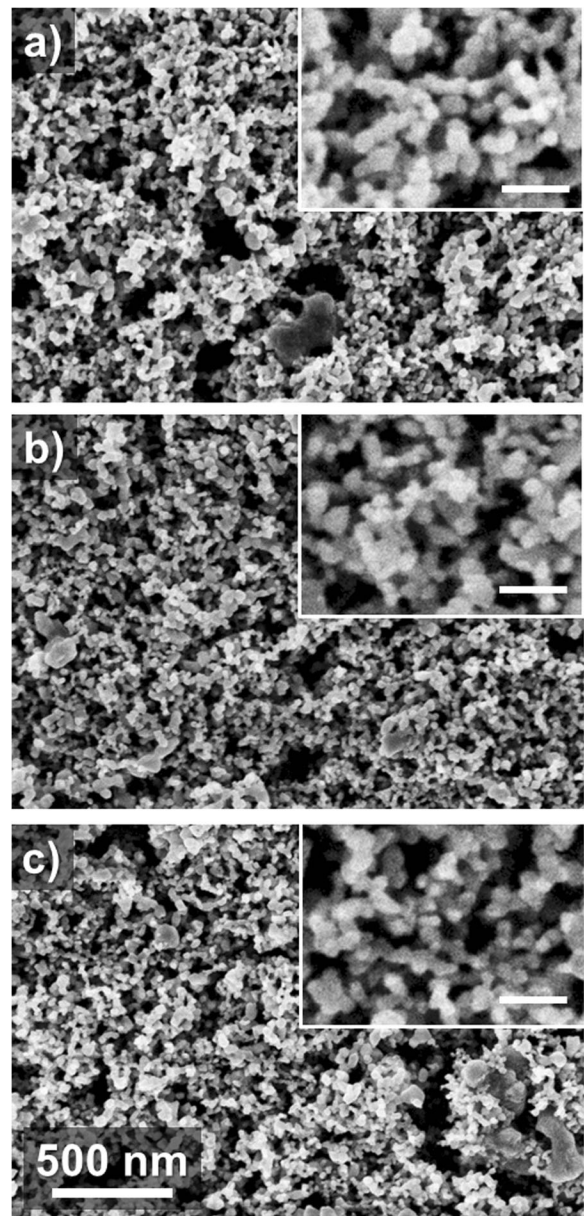
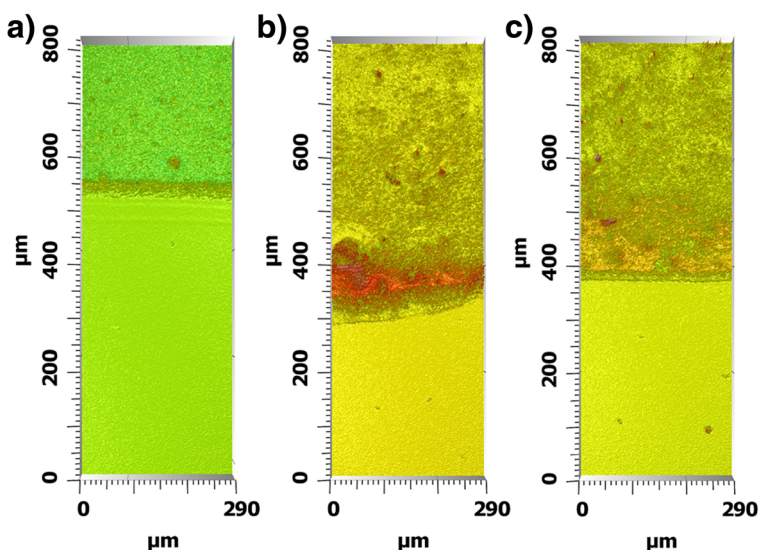


Fig. 4 SEM images of the dip-coated films: **a** TiO₂-Ref, **b** NR-1, and **c** NR-2. Insets: Higher magnification of the structure showing the connectivity of the particles (scale bar: 50 nm)

the TiO₂ portion originating from the titanium isopropoxide functions as a binder.

In order to further compare the surface roughness and topography of the different samples, scanning white-light interferometry (SWLI) was used on samples where only one dip coating/heating cycle has been used. From the images in Fig. 5, somewhat larger variations in the surface structure can be seen between

Fig. 5 SWLI images of dip-coated films on glass slides: **a** TiO₂-Ref, **b** NR-1, and **c** NR-2. The smooth bottom parts depicts the bare FTO substrate, while the thicker and coarser upper parts shows the single layer dip-coated films



the samples compared to the SEM analysis. The reference TiO₂ sample (TiO₂-Ref) appears to have a more uniform structure than the films containing gold nanorods (NR-1 and NR-2). We believe these structural differences arise either from the titanium isopropoxide reacting with trace amounts of reactants remaining from the core-shell nanoparticle synthesis or from a negative effect of the added Au@SiO₂ nanoparticles on the grain coalescence and diffusion process during the formation of the TiO₂ matrix (Epifani et al. 2008). This will affect the particle binding and film formation, and could be a possible reason for the larger roughness of the plasmonic films.

Nevertheless, the SWLI measurements (summarized in Table 2) suggest that after one dip coating/heating cycle, the film thicknesses are comparable (samples TiO₂-Ref and NR-1 have a thickness of $\sim 0.7 \mu\text{m}$, while NR-2 is slightly thicker $\sim 0.8 \mu\text{m}$). However, the inhomogeneities of the plasmonic films can also indirectly

be seen from the much larger standard deviations of these samples. Due to the high porosity, we were not able to interpret the SWLI results of the final four-layer films in a meaningful way. Thus, AFM was used to estimate the thickness of the final film. From Table 2, it is obvious that the thickness of sample NR-1 is slightly thinner ($\sim 1 \mu\text{m}$) than for the other two ($1.6\text{--}1.7 \mu\text{m}$). However, one has to remember that AFM is limited to small sampling areas, so these values should only be taken as indicative. A more global and meaningful approach is to use krypton physisorption to compare the projected surface areas between the different samples. As seen in Table 2, the TiO₂-Ref and NR-2 samples clearly display larger projected surface areas ($\sim 0.26 \text{ m}^2/\text{cm}^2$) compared to sample NR-1 ($\sim 0.14 \text{ m}^2/\text{cm}^2$). This difference in film thickness and projected surface area is important in the following device performance part, as it affects the amount of dye adsorbed onto the photoanode and thus also the

Table 2 Structural properties and dye loading capacity of the produced films. The indicated standard errors are based on 3–4 films

Sample	SWLI one layer thickness (μm)	AFM thickness (μm)	Kr surface area ^a (m^2/cm^2)	Kr surface area ^b (m^2/mm^3)	Dye amount ^a ($\times 10^{-8} \text{ mol}/\text{cm}^2$)	Dye amount ^b ($\times 10^{-7} \text{ mol}/\text{mm}^3$)
TiO ₂ -Ref	0.69 ± 0.07	1.6 ± 0.3	0.26^c	1.7 ± 0.4	2.13 ± 0.76	1.37 ± 0.56
NR-1	0.71 ± 0.22	1.0 ± 0.2	0.14^c	1.4 ± 0.4	1.83 ± 0.08	1.81 ± 0.39
NR-2	0.81 ± 0.32	1.7 ± 0.2	0.26^c	1.5 ± 0.1	1.22 ± 0.15	0.71 ± 0.12

^a Per projected area

^b Per volume

^c The standard error is smaller than $0.01 \text{ m}^2/\text{cm}^2$

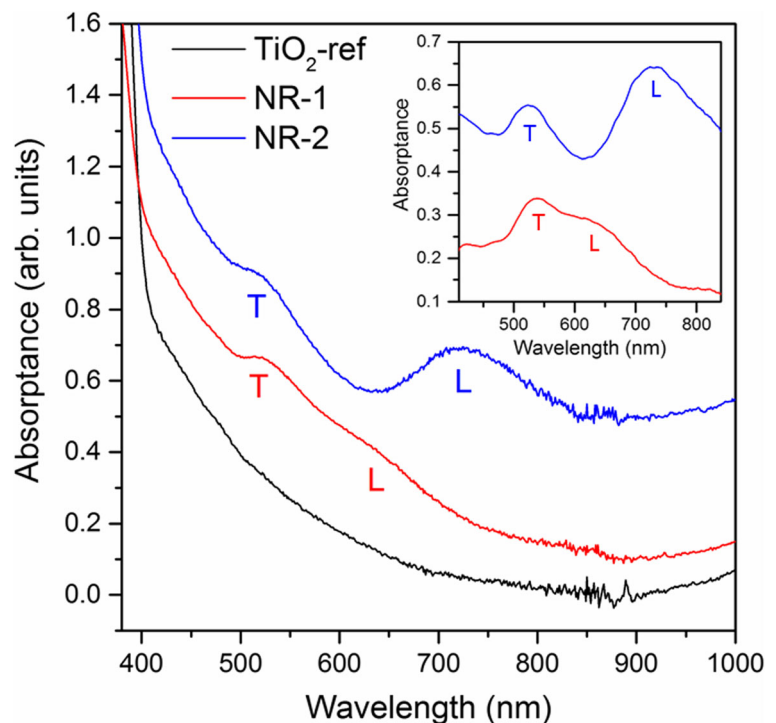
performance of the device. As expected, the Kr surface area per volume is similar in all cases ($\sim 1.5 \text{ m}^2/\text{mm}^3$).

Dye desorption studies by UV-vis were carried out to shed more light on differences in film thickness, roughness, porosity, and/or surface area (see Table 2). These measurements show that there is a fairly large variation in the amount of N719 dye that is adsorbed on these films. From the absorption values at 520 nm, the amount of dye (per projected area) is the highest for the TiO_2 -Ref sample ($2.13 \times 10^{-8} \text{ mol}/\text{cm}^2$), while clearly lower values for the NR-1 and NR-2 photoanodes can be observed ($1.83 \times 10^{-8} \text{ mol}/\text{cm}^2$ and $1.22 \times 10^{-8} \text{ mol}/\text{cm}^2$, respectively). One should remember that the carboxylic anchoring groups of the N719 dye molecules have a strong affinity to TiO_2 surfaces but not to silica. Thus, the inconsistently lower dye desorption value (per volume) observed for the NR-2 sample could partially be explained by that some of the surface area of these films originates from the silica-coated Au NRs. The dye desorption and subsequent UV-vis measurements are considered to be a more reliable measure of the dye loading of the films than the other methods listed in Table 2. Besides the deviations in film thickness, also the influence of porosity and/or limited access to the

TiO_2 surface could impair the estimation of the dye amount in those cases.

In the absorbance spectra in Fig. 6, the TiO_2 reference sample shows the characteristic behavior of absorbing below 400 nm. In the two samples with added Au NRs, both the transverse (T) and longitudinal (L) peaks can be observed even after the particles have been sintered at 200 °C. The transverse plasmon peaks are slightly red-shifted (maxima between 525 and 540 nm) compared to when the particles were dispersed in solution ($\sim 520 \text{ nm}$). Such a shift is typical when the particles are immobilized in a TiO_2 matrix on glass slides resulting in a higher dielectric constant in the surroundings of the particles (Törngren et al. 2014). On the other hand, the longitudinal peaks are clearly blue-shifted compared to the particles in solution (see Table 1). This may indicate a slight deformation of the particles in the TiO_2 matrix even at these lower processing temperatures. This is also in agreement with observations by Petrova et al. (2006), where a deformation was observed already at 200 °C. However, since the TiO_2 matrix requires sintering to ensure sufficient particle interconnectivity and good photoanode performance, a slight deformation of the particles seems unavoidable.

Fig. 6 Absorbance spectra of the dip-coated TiO_2 films without or with added gold nanoparticles (the spectra have been offset for clarity). Inset: Absorbance spectra of the NR-1 and NR-2 samples from where the TiO_2 -Ref sample has been subtracted. The letter “T” indicates the transverse plasmon peaks, while “L” indicates the longitudinal plasmon peaks



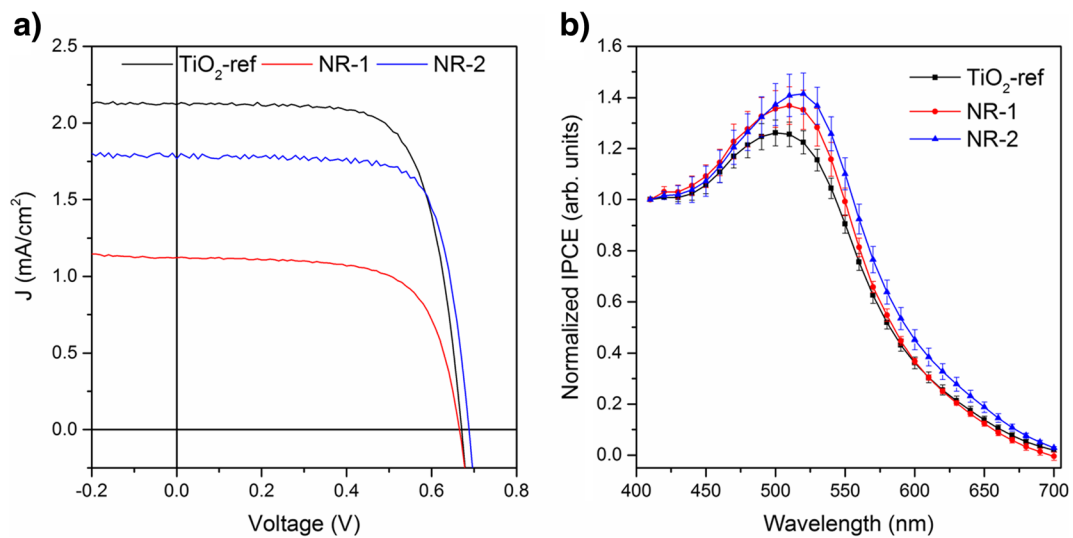


Fig. 7 **a** Representative J-V curves for the different samples and **b** averaged IPCE spectra which have been normalized at 410 nm ($n = 3-4$)

Photovoltaic properties

The impact of the added plasmonic nanoparticles on the photovoltaic properties of DSSCs was studied using the standard N719 dye as the sensitizer. Representative J-V curves and averaged device parameters are shown in Fig. 7a and Table 3, respectively. Compared to champion DSSCs reported in the literature (Albero et al. 2015), the power conversion efficiencies (PCEs) of these devices are comparably low (below 1%). While the open current voltages (V_{OC}) and the fill factors (FF) are comparable to previous reports (Brown et al. 2011; Gangishetty et al. 2013; Törngren et al. 2014), the short-circuit currents (J_{SC}) are generally lower in our devices. The low J_{SC} is due to the relatively thin and highly porous TiO_2 photoanode structures used in our devices, which allows for less dye molecules adsorbed per projected area compared to in previous reports (Bai et al. 2014; Zhang et al. 2006; Johansson et al. 2014). Another reason for the low J_{SC} values could be related to poor electron transport through the TiO_2 material that links the TiO_2 NPs together. This is in good agreement with the studies by Lee et al. (2011) and Nakade et al.

(2002), where the annealing conditions affected the electron transport and lifetime in the TiO_2 films. Similar device performance as in the current study was also seen by Nakade et al. (2002), where 2- μ m-thick TiO_2 films annealed at 150 °C resulted in ~1.5% efficiencies.

It was expected that incorporating the Au@ SiO_2 NPs into the photoanodes would improve the performance of the DSSCs due to an increase in the electric field close to the dye molecule (Sandén et al. 2015; Bai et al. 2014; Chang et al. 2012; Catchpole and Polman 2008). However, from the averaged device parameters listed in Table 3, it is evident that the plasmonic devices perform slightly worse (NR-1) or just equally good (NR-2) as compared to the reference film (TiO_2 -Ref). In any case, no clear improvement (i.e., plasmon enhancement) of the devices can be seen. A large contribution to the discrepancies between these samples can be traced back to the varying J_{SC} values, which is caused by the already mentioned variations in the optical density of the films (i.e., the amount of dye per projected area). If correcting for this, one would obtain higher J_{SC} and PCE values for the plasmonic devices compared to the reference sample. For instance, by correcting for the

Table 3 Statistics of the photovoltaic device parameters ($n = 3-4$)

Sample	J_{sc} (mA/cm ²)	V_{oc} (V)	Fill factor	Efficiency (%)	IPCE peak maximum (nm)
TiO ₂ -Ref	1.8 ± 0.4	0.68 ± 0.02	0.71 ± 0.03	0.88 ± 0.10	502.4 ± 4.2
NR-1	1.1 ± 0.1	0.68 ± 0.02	0.68 ± 0.02	0.52 ± 0.06	510.2 ± 2.3
NR-2	1.8 ± 0.1	0.69 ± 0.01	0.73 ± 0.01	0.90 ± 0.04	516.5 ± 3.2

lower amount of dye adsorbed on the NR-2 sample, the J_{SC} would actually increase by $\sim 70\%$.

More meaningful information about the behavior of the plasmonic particles in the DSSCs can be extracted from the IPCE spectra of the assembled cells. From the raw IPCE data (Fig. S3 in the Supplementary Information), no clear increase in the total conversion efficiency can be seen when introducing plasmonic nanoparticles to the photoanodes. The IPCE spectra display a similar trend as in the J-V curves (i.e., TiO_2 -Ref \sim NR-2 > NR-1), which can mainly be attributed to differences in the thickness or the porosity of the photoanode layers. Nonetheless, it is possible to see a clear enhancement in the 450–700 nm wavelength range from the normalized IPCE spectra in Fig. 7b. The spectra have been normalized at 410 nm where the influence of TiO_2 should be minimal. The peak maximum is slightly red-shifted and the shape is becoming more asymmetric with added $Au@SiO_2$ NRs and increasing aspect ratio (see Table 3). Note that even the maximum for the reference sample is slightly red-shifted compared to the absorption maximum of the N719 dye (~ 496 nm). The peak maximum is located at 502.4 ± 4.2 nm for the TiO_2 -Ref series, but increases to 510.2 ± 2.3 and 516.5 ± 3.2 nm for the NR-1 and NR-2 series, respectively. This indicates that anisotropic nanoparticles with the longitudinal plasmonic peaks (corresponding better to the absorption tail of the dye at higher wavelengths) can be used to improve the performance of DSSCs in the red region of the visible light spectrum. Here we want to stress that similar shifts in the IPCE spectra were not observed in previous studies where anisotropic nanorods have been used in DSSCs (Bai et al. 2014; Chang et al. 2012). This is most likely explained by a transition from a rod-like to a spherical shape of the plasmonic particles due to the high sintering temperatures applied in those studies (i.e., 500 °C). On the contrary, by using the low-temperature processing protocol in our work (maximum processing temperature of 200 °C), this structural deformation can be avoided.

Conclusions

The overall aim of the study was to investigate and improve the performance of DSSCs by plasmon enhancement in the sub-NIR region by utilizing gold nanorods. Two types of plasmonic core-shell gold nanorods with different aspect ratios were successfully

synthesized using wet chemical methods. These particles showed clear optical responses in the visible range at 520 and 700 nm as well as 520 and 800 nm, respectively. The particles were coated with a thin SiO_2 shell, in order to protect them from dissolving in the electrolyte as well as to prevent charge recombination. UV-vis and TEM studies showed that the $Au@SiO_2$ NRs are thermally stable up to at least 200 °C. Mesoporous TiO_2 films containing plasmonic gold nanoparticles were prepared using sol-gel methods enabling low-temperature processing. By using a range of structural characterization techniques, we were able to determine how the addition of the $Au@SiO_2$ nanorods affected the structure of the produced films. The performance of these films as photoanodes in DSSCs was evaluated. When taking the differences in the amount of N719 dye per projected area into account, it is evident that the plasmonic particles would cause an enhancement of the J_{SC} values. Furthermore, the IPCE spectra reveal a clear red shift of the peak in the 500–520 nm range and, after normalizing the spectra, an enhancement in the 500–700 nm wavelength range for the samples containing the $Au@SiO_2$ NRs. We believe these observations can be directly associated with the LSPR peaks for the gold nanorods. Thus, the minimal structural deformation of the gold nanorods using the presented low-temperature processing protocol allowed us to demonstrate the potential of using $Au@SiO_2$ NRs to enhance the performance of DSSCs in the sub-NIR wavelength range.

Funding This study was funded by the Academy of Finland (grant numbers 259310, 271081, and 279055) and the Tiina and Antti Herlin Foundation (personal grant for A.T.).

Compliance with ethical standards

Conflict of interest The authors declare that they have no conflict of interest.

References

- Albero J, Atienzar P, Corma A, Garcia H (2015) Efficiency records in mesoscopic dye-sensitized solar cells. *Chem Rec* 15:803–828. <https://doi.org/10.1002/tcr.201500007>
- Alvarez-Puebla R, Liz-Marzán LM, García de Abajo FJ (2010) Light concentration at the nanometer scale. *J Phys Chem Lett* 1:2428–2434. <https://doi.org/10.1021/jz100820m>
- Atwater HA, Polman A (2010) Plasmonics for improved photovoltaic devices. *Nat Mater* 9:205–213. <https://doi.org/10.1038/nmat2629>

- Bai L, Li M, Guo K, Luoshan M, Mehnane HF, Pei L, Pan M, Liao L, Zhao X (2014) Plasmonic enhancement of the performance of dye-sensitized solar cell by core-shell AuNRs@SiO₂ in composite photoanode. *J Power Sources* 272:1100–1105. <https://doi.org/10.1016/j.jpowsour.2014.09.083>
- Bohren CF, Huffman DR (2004) Absorption and scattering of light by small particles. John Wiley & Sons Inc. WILEY-VCH Verlag GmbH & Co. KGaA, Weinheim. <https://doi.org/10.1002/9783527618156>
- Brown MD, Suteewong T, Kumar RSS, D'Innocenzo V, Petrozza A, Lee MM, Wiesner U, Snaith HJ (2011) Plasmonic dye-sensitized solar cells using core-shell metal-insulator nanoparticles. *Nano Lett* 11:438–445. <https://doi.org/10.1021/nl1031106>
- Carretero-Palacios S, Calvo ME, Míguez H (2015) Absorption enhancement in organic-inorganic halide perovskite films with embedded plasmonic gold nanoparticles. *J Phys Chem C* 119: 18635–18640. <https://doi.org/10.1021/acs.jpcc.5b06473>
- Catchpole KR, Polman A (2008) Plasmonic solar cells. *Opt Express* 16:21793. <https://doi.org/10.1364/OE.16.021793>
- Chang S, Li Q, Xiao X, Wong KY, Chen T (2012) Enhancement of low energy sunlight harvesting in dye-sensitized solar cells using plasmonic gold nanorods. *Energy Environ Sci* 5:9444–9448. <https://doi.org/10.1039/C2EE22657J>
- Cong H, Toftegaard R, Ambjerg J, Ogilby PR (2010) Silica-coated gold nanorods with a gold overcoat: controlling optical properties by controlling the dimensions of a gold-silica-gold layered nanoparticle. *Langmuir* 26:4188–4195. <https://doi.org/10.1021/la9032223>
- de Aberasturi DJ, Serrano-Montes AB, Liz-Marzán LM (2015) Modern applications of plasmonic nanoparticles: from energy to health. *Adv Opt Mater* 3:602–617. <https://doi.org/10.1002/adom.201500053>
- Epifani M, Helwig A, Arbiol J, Díaz R, Francioso L, Siciliano P, Mueller G, Morante JR (2008) TiO₂ thin films from titanium butoxide: synthesis, Pt addition, structural stability, micro-electronic processing and gas-sensing properties. *Sensors Actuators B Chem* 130:599–608. <https://doi.org/10.1016/j.snb.2007.10.016>
- Erwin WR, Zarick HF, Talbert EM, Bardhan R (2016) Light trapping in mesoporous solar cells with plasmonic nanostructures. *Energy Environ Sci* 9:1577–1601. <https://doi.org/10.1039/C5EE03847B>
- Gangishetty MK, Lee KE, Scott RWJ, Kelly TL (2013) Plasmonic enhancement of dye sensitized solar cells in the red-to-near-infrared region using triangular core-shell Ag@SiO₂ nanoparticles. *ACS Appl Mater Interfaces* 5:11044–11051. <https://doi.org/10.1021/am403280r>
- Gu M, Ouyang Z, Jia B, Stokes N, Chen X, Fahim N, Li X, Ventura MJ, Shi Z (2012) Nanoplasmonics: a frontier of photovoltaic solar cells. *Nano* 1:235–248. <https://doi.org/10.1515/nanoph-2012-0180>
- Guerrero-Martínez A, Pérez-Juste J, Liz-Marzán LM (2010) Recent progress on silica coating of nanoparticles and related nanomaterials. *Adv Mater* 22:1182–1195. <https://doi.org/10.1002/adma.200901263>
- Hou W, Cronin SB (2013) A review of surface plasmon resonance-enhanced photocatalysis. *Adv Funct Mater* 23: 1612–1619. <https://doi.org/10.1002/adfm.201202148>
- Jang YH, Jang YJ, Kim S, Quan LN, Chung K, Kim DH (2016) Plasmonic solar cells: from rational design to mechanism overview. *Chem Rev* 116:14982–15034. <https://doi.org/10.1021/acs.chemrev.6b00302>
- Johansson V, Ellis-Gibbins L, Clarke T, Gorlov M, Andersson GG, Kloo L (2014) On the correlation between dye coverage and photoelectrochemical performance in dye-sensitized solar cells. *Phys Chem Chem Phys* 16:711–718. <https://doi.org/10.1039/C3CP52486H>
- Kale MJ, Avanesian T, Christopher P (2014) Direct photocatalysis by plasmonic nanostructures. *ACS Catal* 4:116–128. <https://doi.org/10.1021/cs400993w>
- Khlebtsov NG, Dykman LA (2010) Optical properties and biomedical applications of plasmonic nanoparticles. *J Quant Spectrosc Radiat Transf* 111:1–35. <https://doi.org/10.1016/j.jqsrt.2009.07.012>
- Kim H, Hwang T (2014) Effect of titanium isopropoxide addition in low-temperature cured TiO₂ photoanode for a flexible DSSC. *J Sol-Gel Sci Technol* 72:67–73. <https://doi.org/10.1007/s10971-014-3427-0>
- Koenderink AF, Alù A, Polman A (2015) Nanophotonics: shrinking light-based technology. *Science* 348:516–521. <https://doi.org/10.1126/science.1261243>
- Lee C-R, Kim H-S, Park N-G (2011) Dependence of porosity, charge recombination kinetics and photovoltaic performance on annealing condition of TiO₂ films. *Front Optoelectron China* 4:59–64. <https://doi.org/10.1007/s12200-011-0205-2>
- Liu B-J, Lin K-Q, Hu S, Wang X, Lei Z-C, Lin H-X, Ren B (2015) Extraction of absorption and scattering contribution of metallic nanoparticles toward rational synthesis and application. *Anal Chem* 87:1058–1065. <https://doi.org/10.1021/ac503612b>
- Long R, Li Y, Song L, Xiong Y (2015) Coupling solar energy into reactions: materials design for surface plasmon-mediated catalysis. *Small* 11:3873–3889. <https://doi.org/10.1002/smll.201403777>
- Motl NE, Smith AF, DeSantis CJ, Skrabalak SE (2014) Engineering plasmonic metal colloids through composition and structural design. *Chem Soc Rev* 43:3823–3834. <https://doi.org/10.1039/C3CS60347D>
- Murphy CJ, Sau TK, Gole AM, Orendorff CJ, Gao J, Gou L, Hunyadi SE, Li T (2005) Anisotropic metal nanoparticles: synthesis, assembly, and optical applications. *J Phys Chem B* 109:13857–13870. <https://doi.org/10.1021/jp0516846>
- Nakade S, Matsuda M, Kambe S, Saito Y, Kitamura T, Sakata T, Wada Y, Mori H, Yanagida S (2002) Dependence of TiO₂ nanoparticle preparation methods and annealing temperature on the efficiency of dye-sensitized solar cells. *J Phys Chem B* 106:10004–10010. <https://doi.org/10.1021/jp020051d>
- Nikoobakht B, El-Sayed MA (2003) Preparation and growth mechanism of gold nanorods (NRs) using seed-mediated growth method. *Chem Mater* 15:1957–1962. <https://doi.org/10.1021/cm020732l>
- Obare SO, Jana NR, Murphy CJ (2001) Preparation of polystyrene- and silica-coated gold nanorods and their use as templates for the synthesis of hollow nanotubes. *Nano Lett* 1:601–603. <https://doi.org/10.1021/nl0156134>
- Pérez-Juste J, Pastoriza-Santos I, Liz-Marzán LM, Mulvaney P (2005) Gold nanorods: synthesis, characterization and applications. *Coord Chem Rev* 249:1870–1901. <https://doi.org/10.1016/j.ccr.2005.01.030>

- Petrova H, Juste JP, Pastoriza-Santos I, Hartland GV, Liz-Marzán LM, Mulvaney P (2006) On the temperature stability of gold nanorods: comparison between thermal and ultrafast laser-induced heating. *Phys Chem Chem Phys* 8:814–821. <https://doi.org/10.1039/B514644E>
- Pillai S, Green MA (2010) Plasmonics for photovoltaic applications. *Sol Energy Mater Sol Cells* 94:1481–1486. <https://doi.org/10.1016/j.solmat.2010.02.046>
- Sandén S, Akitsu K, Törngren B, Ylinen A, Smått J-H, Kubo T, Matsumura M, Otani N, Segawa H, Österbacka R (2015) Plasmon-enhanced polymer-sensitized solar cells. *J Phys Chem C* 119:5570–5576. <https://doi.org/10.1021/jp5097458>
- Scarabelli L, Sánchez-Iglesias A, Pérez-Juste J, Liz-Marzán LM (2015) A “tips and tricks” practical guide to the synthesis of gold nanorods. *J Phys Chem Lett* 6:4270–4279. <https://doi.org/10.1021/acs.jpcclett.5b02123>
- Schuller JA, Barnard ES, Cai W, Jun YC, White JS, Brongersma ML (2010) Plasmonics for extreme light concentration and manipulation. *Nat Mater* 9:193–204. <https://doi.org/10.1038/nmat2630>
- Smith JG, Faucheaux JA, Jain PK (2015) Plasmon resonances for solar energy harvesting: a mechanistic outlook. *Nano Today* 10:67–80. <https://doi.org/10.1016/j.nantod.2014.12.004>
- Sotiriou GA (2013) Biomedical applications of multifunctional plasmonic nanoparticles. *Wiley Interdiscip Rev: Nanomed Nanobiotechnol* 5:19–30. <https://doi.org/10.1002/wnan.1190>
- Standridge SD, Schatz GC, Hupp JT (2009) Toward plasmonic solar cells: protection of silver nanoparticles via atomic layer deposition of TiO₂. *Langmuir* 25:2596–2600. <https://doi.org/10.1021/la900113e>
- Tokel O, Inci F, Demirci U (2014) Advances in plasmonic technologies for point of care applications. *Chem Rev* 114:5728–5752. <https://doi.org/10.1021/cr4000623>
- Törngren B, Akitsu K, Ylinen A, Sandén S, Jiang H, Ruokolainen J, Komatsu M, Hamamura T, Nakazaki J, Kubo T, Segawa H, Österbacka R, Smått J-H (2014) Investigation of plasmonic gold–silica core–shell nanoparticle stability in dye-sensitized solar cell applications. *J Colloid Interface Sci* 427:54–61. <https://doi.org/10.1016/j.jcis.2013.11.085>
- Wang J, Lee Y-J, Chadha AS, Yi J, Jespersen ML, Kelley JJ, Nguyen HM, Nimmo M, Malko AV, Vaia RA, Zhou W, Hsu JWP (2012) Effect of plasmonic Au nanoparticles on inverted organic solar cell performance. *J Phys Chem C* 117: 85–97. <https://doi.org/10.1021/jp309415u>
- Wong TKS (2017) Effect of embedded nanoparticle surface chemistry on plasmonic organic photovoltaic devices. *Mater Renew Sustain Energy* 6:4. <https://doi.org/10.1007/s40243-017-0087-3>
- Ye Y, Jo C, Jeong I, Lee J (2013) Functional mesoporous materials for energy applications: solar cells, fuel cells, and batteries. *Nano* 5:4584–4605. <https://doi.org/10.1039/C3NR00176H>
- Zayats AV, Smolyaninov II (2003) Near-field photonics: surface plasmon polaritons and localized surface plasmons. *J Opt A Pure Appl Opt* 5:S16. <https://doi.org/10.1088/1464-4258/5/4/353>
- Zhang D, Yoshida T, Oekermann T, Furuta K, Minoura H (2006) Room-temperature synthesis of porous nanoparticulate TiO₂ films for flexible dye-sensitized solar cells. *Adv Funct Mater* 16:1228–1234. <https://doi.org/10.1002/adfm.200500700>
- Zhang R, Zhou Y, Peng L, Li X, Chen S, Feng X, Guan Y, Huang W (2016) Influence of SiO₂ shell thickness on power conversion efficiency in plasmonic polymer solar cells with Au nanorod@SiO₂ core-shell structures. *Sci Rep* 6:25036. <https://doi.org/10.1038/srep25036>